

Linköping University Post Print

Direct evidence of detwinning in polycrystalline Ni-Mn-Ga ferromagnetic shape memory alloys during deformation

Z H Nie, Ru Peng, Sten Johansson, E C Oliver, Y Ren, Y D Wang, Y D Liu,

J N Deng, L Zuo and D E Brown

N.B.: When citing this work, cite the original article.

Original Publication:

Z H Nie, Ru Peng, Sten Johansson, E C Oliver, Y Ren, Y D Wang, Y D Liu, J N Deng, L Zuo and D E Brown, Direct evidence of detwinning in polycrystalline Ni-Mn-Ga ferromagnetic shape memory alloys during deformation, 2008, JOURNAL OF APPLIED PHYSICS, (104), 10, 103519.

<http://dx.doi.org/10.1063/1.3020534>

Copyright: American Institute of Physics

<http://www.aip.org/>

Postprint available at: Linköping University Electronic Press

<http://urn.kb.se/resolve?urn=urn:nbn:se:liu:diva-16617>

Direct evidence of detwinning in polycrystalline Ni–Mn–Ga ferromagnetic shape memory alloys during deformation

Z. H. Nie,¹ R. Lin Peng,² S. Johansson,² E. C. Oliver,³ Y. Ren,⁴ Y. D. Wang,^{1,a)} Y. D. Liu,¹ J. N. Deng,¹ L. Zuo,¹ and D. E. Brown⁵

¹Key Laboratory for Anisotropy and Texture of Materials (Ministry of Education), Northeastern University, Shenyang 110004, China

²Department of Mechanical Engineering, Linköping University, S-58183 Linköping, Sweden

³Rutherford Appleton Laboratory, Chilton, Didcot, Oxon OX11 0QX, United Kingdom

⁴X-ray Sciences Division, Argonne National Laboratory, Argonne, Illinois 60439, USA

⁵Department of Physics, Northern Illinois University, DeKalb, Illinois 60115, USA

(Received 4 March 2008; accepted 28 September 2008; published online 19 November 2008)

In situ time-of-flight neutron diffraction and high-energy x-ray diffraction techniques were used to reveal the preferred reselection of martensite variants through a detwinning process in polycrystalline Ni–Mn–Ga ferromagnetic shape memory alloys under uniaxial compressive stress. The variant reorientation via detwinning during loading can be explained by considering the influence of external stress on the grain/variant orientation-dependent distortion energy. These direct observations of detwinning provide a good understanding of the deformation mechanisms in shape memory alloys. © 2008 American Institute of Physics. [DOI: 10.1063/1.3020534]

I. INTRODUCTION

Ferromagnetic shape memory alloys (SMAs) such as Ni–Mn–Ga,^{1–3} Fe–Pt,⁴ and (NiCo)–Mn–In^{5,6} have received great attention due to their giant magnetic-field-induced strain (MFIS) and shape memory effect (SME). The MFIS is achieved through a reorientation of martensitic variants (motion of twin boundaries) where their easy magnetization axis becomes aligned along an applied magnetic field.⁷ For the Ni–Mn–Ga(In) alloy system, detwinning is an important process that plays a crucial role in controlling the MFIS. In spite of previous experimental investigations on the external-field-induced strain in alloys such as Ni–Ti (Ref. 8) and Ni–Mn–Ga,⁹ the physical mechanisms behind the detwinning process, particularly regarding the intrinsic physical nature of variant selection, are far from fully understood. Neutron diffraction and high-energy x-ray diffraction techniques provide effective methods for *in situ* studies of deformation processes in SMAs, such as Ni–Ti,^{10,11} FePd,^{12,13} and Ni–Mn–Ga,^{14–18} under various loading and/or heating conditions. In this work, the principles of the detwinning mechanism under a uniaxial loading of Ni–Mn–Ga SMAs are revealed. The chosen Ni–Mn–Ga alloy has a simple (tetragonal) structure with a large c/a value, which makes it an ideal target for the investigation of variant-selection-mediated plasticity in materials with a high anisotropy.

II. EXPERIMENT

A Ni–Mn–Ga ingot with a nominal chemical composition of 49% Ni, 25% Mn, 22% Ga, and 4% Co in atomic percent was prepared by the arc-melting method. A part of the ingot was then cast into an ice-water cooled copper mold, and subsequently a rod of 7 mm in diameter and 20 mm in length was cut by a spark machine. Neutron diffraction ex-

periments on the rod show that the specimen has a nonmodulated martensitic structure ($I4/mmm$) at room temperature with $a=3.897$ Å and $c=6.438$ Å.¹⁸ Two rectangular specimens 2.0 mm (height) \times 2.0 mm (width) \times 4.0 mm (longitudinal) were cut from the other part of the polycrystalline ingot, one of which was used for high-energy x-ray diffraction experiments. The other specimen was polished and placed on a small dedicated loading device mounted on a JOEL-7001F scanning electron microscope (SEM) for observing the *in situ* change in the microstructural characteristics (including grain size, twinning, etc.) under the compression deformation. The amount of deformation was controlled with a screw that adjusted the displacement of two headers attached on the two sides of the specimen.

In situ neutron diffraction experiments on the rod were performed on the ENGIN-X engineering diffractometer at the ISIS spallation neutron source to study the uniaxial compressive loading/unloading process. Time-of-flight neutron diffraction patterns were collected simultaneously by two $\pm 90^\circ$ detector banks with a hold time of ~ 55 min at each load level. The load axis was aligned horizontally at 45° to the incident beam so that the two scattering vectors (observed by the $\pm 90^\circ$ detector banks, respectively) were parallel or perpendicular to the loading direction (LD), respectively.¹⁹ The incident neutron beam slit was 4×7 mm². The *in situ* loading experiment was performed at room temperature with the loading stress incremented stepwise from -5 to -250 MPa and then decreased stepwise to -5 MPa. Subsequently, the specimen was heated up to 513 K from room temperature under a stress of -5 MPa to study the recovery of plastic strain. The general structural analysis software (GSAS) (Ref. 20) was used for neutron data reduction. While the different (hkl) lattice strains were determined by fitting individual diffraction peaks, the neutron spectra collected by the two detector banks were fitted by GSAS to refine the lattice parameters, absorption, background, and the

^{a)}Electronic mail: ydwang@mail.neu.edu.cn.

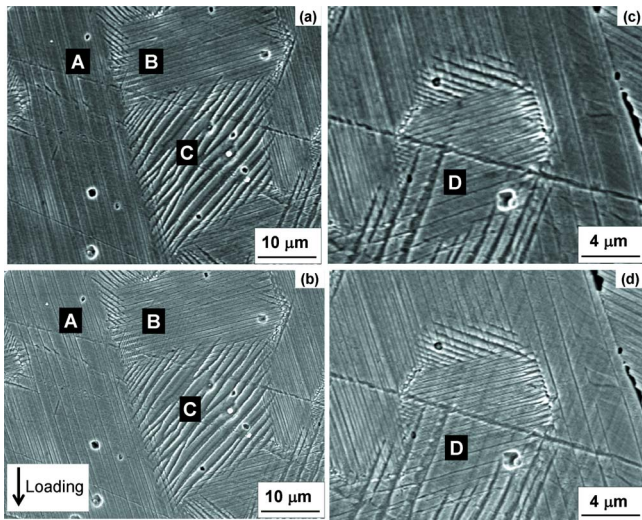


FIG. 1. (Color online) SEM micrographs of the Ni–Mn–Ga ingot [(a) and (c)] before and [(b) and (d)] after deformation ($\epsilon=4\%$).

harmonic texture coefficients $T_{ln}(L_{\max}=10)$. Here the fiber symmetry along the LD of the specimen was verified by collecting the diffraction patterns using the detector bank (with the scattering vector) along the transverse direction while the specimen was rotated to different angles around the LD. Inverse pole figure (IPF) along the LD, i.e., $Q(\chi, \eta)$, which enables changes in the distribution of variants during loading and unloading to be quantitatively displayed, was thus determined at different loading states²¹

$$Q(\chi, \eta) = \sum_{l=0}^{l=L_{\max}} \sum_{n=-l}^l T_{ln} P_l^n(\cos \chi) \exp(-in\eta), \quad (1)$$

where $P_l^n(x)$ is the associated Legendre function while χ and η are the polar and azimuthal angles. The crystal symmetry is also used to construct the IPF.

The *in situ* high-energy x-ray diffraction experiments were carried out at the 11-ID-C beam line at the Advanced Photon Source, Argonne National Laboratory. This station provided a monochromatic beam of hard x rays (115 keV) having a beam size of 0.8×0.8 mm². The x rays were incident perpendicular to the LD and the measurements were made in transmission geometry. A two-dimensional image plate detector (Mar345) was used to measure the diffracted x rays. Room temperature *in situ* uniaxial loading experiments were performed with the loading stress incremented stepwise from -8 to -217 MPa along the specimen's longitudinal direction. At each loading state, the specimen was rotated around the vertical axial from -4° to $+5^\circ$ in intervals of 1° , which covers nine intervals of reciprocal space to trace the variation in grains along the LD.

III. MICROSTRUCTURES

SEM observations showed that two kinds of twin morphology, i.e., twin variants having straight twin boundaries [zones A and B in Fig. 1(a)] and twin variants having curved twin boundaries [zone C in Fig. 1(a)], exist in the initial (undeformed) Ni–Mn–Ga alloy. The grain size varies from 10 to 50 μm . The thickness of the twin variants having

straight twin boundaries is $1-0.5$ μm , which, as can be seen in Fig. 1(a), is obviously less than that for twin variants having curved twin boundaries. For the specimen under a compressive uniaxial loading (with a total strain of $\sim 4\%$), the twin width was slightly increased in zone A and some new fine twin variants appeared in zone B [as shown in Fig. 1(b)]. Further comparison between the twin morphologies of a small grain (zone D) for the initial and deformed specimens confirmed also the deformation-induced change in the arrangements of twin variants [as shown in Figs. 1(c) and 1(d)]. It was also observed that the change in twin domains strongly depends on the grain orientation or arranged configurations of twin domains. However, a detailed change in some fine microstructures, particularly the nanoscale twins inside the twin domain, cannot be seen by our SEM due to its limited resolution. Thus, we used *in situ* neutron diffraction to study the quantitative change in the statistical distribution of twin variants, and we used *in situ* high-energy x-ray diffraction to study the evolution of twin domains inside individual grains during the deformation.

IV. CHANGE IN THE DISTRIBUTION OF TWIN VARIANTS

The macroscopic stress versus strain curve obtained from neutron diffraction measurements during loading/unloading, as shown in Fig. 2(a), displays three deformation stages during loading: (1) an elastic region (A to B), (2) a lower work-hardening-ratio region (B to C), and (3) a higher work-hardening-ratio region (C to E). The variation in lattice strain with applied load is shown for the (112) and (110) diffraction peaks in Figs. 2(b) and 2(c), respectively. In the elastic region (A to B), an almost linear relationship is observed for both reflections. After entering into the lower work-hardening-ratio region (B to C), a slow increase in the (110) lattice strain and a fluctuation in the (112) lattice strain are observed. Interestingly, a large increase in the (110) lattice strain and almost constant lattice strain for (112) is found in the higher work-hardening-ratio region (C to E). This trend can be well explained by the grain-orientation-dependent selection of detwinning during uniaxial loading. It is well established that the tetragonal structural Ni–Mn–Ga alloy exhibits twins having twinning elements $\mathbf{K}_1 = \{112\}$ and $\boldsymbol{\eta}_1 = \langle 11-1 \rangle$.²² The Schmid factor of the twinning activity is 0.47, 0.31, and 0.23 for grains along $(001) \perp \text{LD}$, $(112) \perp \text{LD}$, and $(110) \perp \text{LD}$, respectively. Thus, the martensitic variants with the a -axis or b -axis along the LD are stable that may grow during compression at the expense of the variants with the c -axis along the LD through a detwinning process (direct evidences shown latter), as evidenced from a large Schmid factor in the grain orientation with the $(001) \perp \text{LD}$ and $(112) \perp \text{LD}$. That is the reason why the lattice strain for the (112) reflection ($\perp \text{LD}$) remains constant in the region of C to E; however, a large elastic lattice strain for the (110) reflection ($\perp \text{LD}$) is required to maintain the strain balance in the polycrystalline material during compression.

A residual macroscopic strain of -3.1% was observed after unloading, whereas the residual lattice strains for the (110) and (112) reflections were -2.500×10^{-6} and $+450$

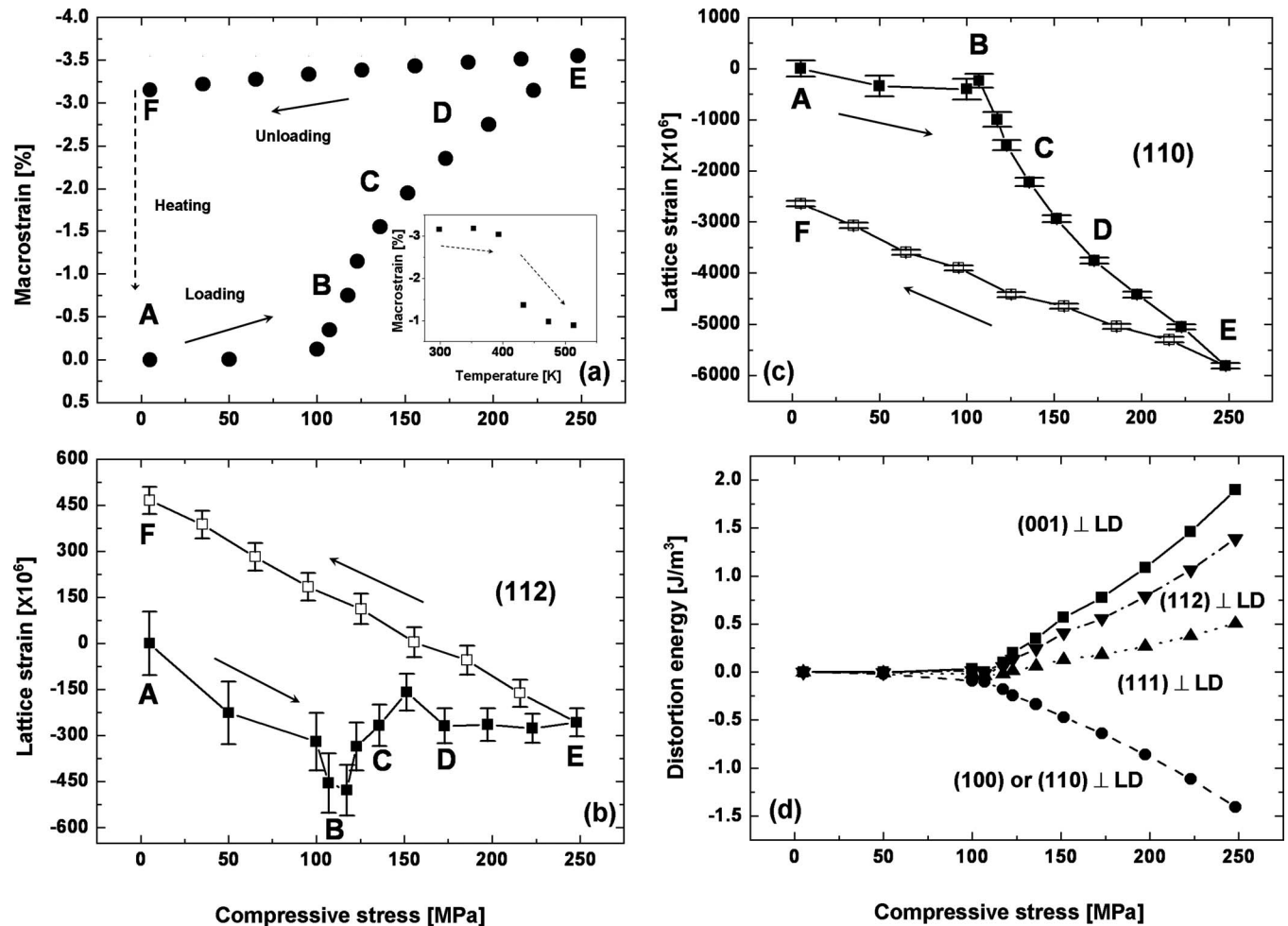


FIG. 2. (a) The macroscopic strain vs stress curve. The inset shows the change in residual macroscopic strain as a function of temperature. (b) The (112) and (c) the (110) lattice strain vs stress curves. (d) Changes in the distortion energy for specified texture components $[(hkl) \perp LD]$ as a function of applied stress. The points A-B-C-D-E-F correspond to the different deformation states.

$\times 10^{-6}$, respectively. The observed -3.1% residual macroscopic strain reduced to -0.9% after the specimen was heated above the austenite finish temperature (450 K), as shown in the inset of Fig. 2(a). This trend indicates that the detwinning state is metastable and the difference in the energy between the stable and metastable states is a driving force for the SME in this alloy.

The IPFs derived from the neutron measurements are given in Fig. 3 for the different deformation stages indicated in Fig. 2. In the initial state (A), the specimen exhibits three main texture components, i.e., $(001) \perp LD$, $(111) \perp LD$, and $(hk0) \perp LD$. The main texture components corresponding to

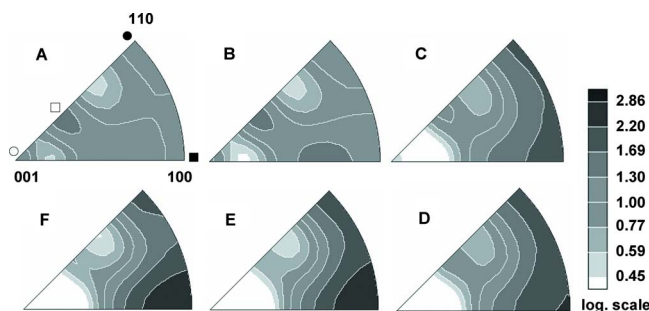


FIG. 3. (Color online) IPFs of the Ni-Mn-Ga alloy at the different deformation states specified in Fig. 2.

the martensitic variants are also given in Fig. 3 with the open and solid circles for $(001) \perp LD$ and $(110) \perp LD$ and the open and solid squares for $(111) \perp LD$ and $(100) \perp LD$, respectively. Loading in the elastic region from points A to B causes a slight decrease in intensities for the (001) and (111) components but an increase for the $(hk0)$ component. The low applied stresses in this elastic region actually cause detwinning through the movement of twin boundaries, as has been observed in single crystals.⁹ For the lower work-hardening-ratio region from B to C, as the detwinning process continues, the intensities of the (001) and (111) components become weaker and the $(hk0)$ component becomes stronger. Eventually, the (001) component vanishes and the (111) component becomes quite weak when entering the higher work-hardening-ratio region from C to E. The detwinning after unloading is not reversed upon unloading, as seen from the unchanged IPF [Fig. 3(f)]. This indicates that the -3.1% residual strain observed after unloading can be attributed to the reoriented variants through the detwinning process.

V. TRACING THE DETWINNING IN INDIVIDUAL GRAINS

High-energy x-ray diffraction has a high resolution and can measure the evolution of just a few grains at certain

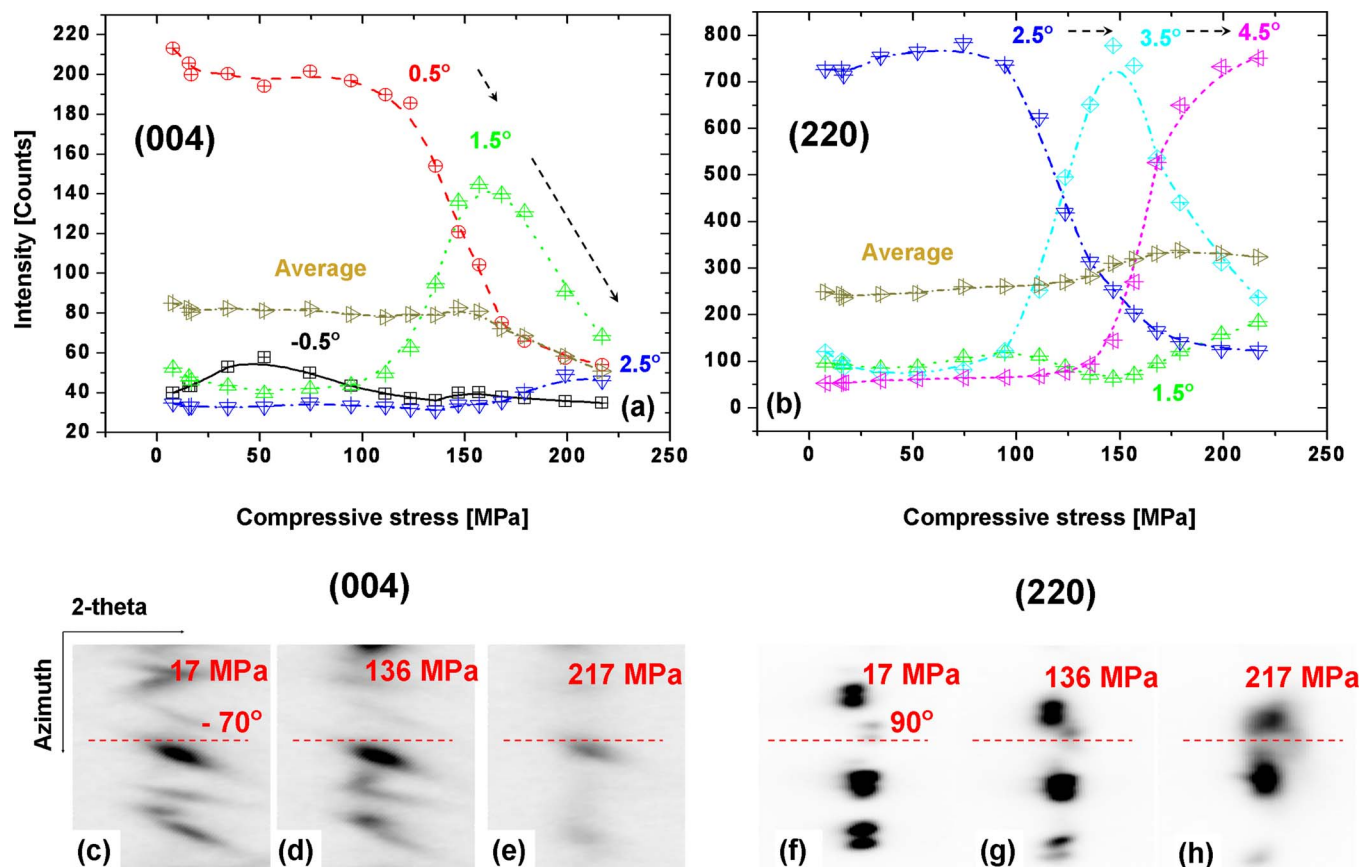


FIG. 4. (Color online) Variations in x-ray intensity of (a) (004) and (b) (220) as a function of compressive stress at a series of sample oscillation angles. The x-ray diffraction image, which was obtained by summing all images collected at different oscillation angles, under different compressive stresses of (c) 17 MPa, (d) 136 MPa, (e) 217 MPa for (004), (f) 17 MPa, (g) 136 MPa, and (h) 217 MPa for (220).

azimuthal angles under deformation. Diffraction spots at certain azimuthal angles, i.e., $\sim -70^\circ$ for (004) and $\sim 90^\circ$ for (220), are selected to display the integral intensity variations at different sample rotation angles η as a function of compressive stress, as shown in Figs. 4(a) and 4(b), respectively. At the same azimuthal intervals, the diffraction spots covering a large $\eta = -4^\circ \sim +5^\circ$ for (004) and (220) are displayed in Figs. 4(c)–4(h). According to the stress versus strain curve obtained from high-energy x-ray diffraction measurements, the specimen is still in the lower work-hardening-ratio region for compressive stresses up to 217 MPa, which is slightly different from the neutron diffraction results [Fig. 2(a)]. The differences can be attributed to the different sample geometries used for the two experiments. It is shown in Figs. 4(a) and 4(b) that the (004) or (220) grains rotate around 2° during the compressive stress from ~ 100 to ~ 200 MPa, which can be seen from the intensity variation at different η . However, the total intensity of (004) grains becomes weaker and that of (220) grains slightly increases, as seen in the average intensity changes in Figs. 4(a) and 4(b) and the evolution of the diffraction spots in Figs. 4(c)–4(h). A rotation of (220) variants to the azimuth angle of $+90^\circ$ during compression was also seen [see Figs. 4(f)–4(h)].

The direct evidences from neutron and x-ray diffraction techniques show that the martensitic variants with the a -axis along the LD grow during compression at the expense of the variants with the c -axis along the LD.⁹ This is the essence of

the detwinning process and it is the way that materials “remember” their original shape during deformation. Detwinning leads to the changes in variants, and this is the main deformation mechanism. However, generation of dislocations will also accrue in the higher work-hardening-ratio region,²³ which cannot recover after being heated above the austenite finish temperature. Dislocations will limit the ability of the SME.

The variant reorientation of the detwinning process during loading can be explained by considering the influence of an external stress on the grain/variant orientation-dependent distortion energy [denoted as $E(g_i)$].¹⁴ The external stress induces a lattice distortion, which may be expressed by three principle strains, i.e., ε_{11} , ε_{22} , and ε_{33} . The variant orientation-dependent distortion energy $E(g_i)$ with external stress σ_{ij} can be expressed as

$$E(g_i) = -\frac{\sigma_{ij} a_{ik} a_{jl} \varepsilon_{kl}}{2}, \quad (2)$$

where a_{ij} is the element of the transformation matrix relating the crystal coordinate system to the sample coordinate system. For some special variant orientations, for example, (001) \perp LD, (111) \perp LD, (100) \perp LD, (110) \perp LD, and (112) \perp LD, $E(g_i)$ has been calculated according to the lattice distortion at different stress levels from neutron diffraction experiments and plotted in Fig. 2(d). This figure shows that the grains with (100) \perp LD and (110) \perp LD exhibit the same

distortion energy with increasing compressive stress. Between -5 and -100 MPa, the difference in distortion energy among the variant orientations is small, and this agrees with the small changes in the IPFs observed at this stage [Figs. 3(a) and 3(b)]. Beyond -100 MPa, with increasing applied compressive stress, the distortion energy increases for grains with $(001) \perp LD$, $(111) \perp LD$, and $(112) \perp LD$ and decreases for grains with $(100) \perp LD$ and $(110) \perp LD$. This may well explain the enhanced density of those grains with $(100) \perp LD$ and $(110) \perp LD$ orientations and the decreased density of the grains with $(001) \perp LD$ and $(111) \perp LD$. It is also found that distortion energy for $(001) \perp LD$ is slightly larger than for $(111) \perp LD$. This trend should correspond to the early decrease in orientation intensity for the grains with $(001) \perp LD$.

VI. CONCLUDING REMARKS

The neutron diffraction and high-energy x-ray diffraction techniques provide direct evidence of the reselection of martensitic variants through detwinning in Ni–Mn–Ga SMAs under a uniaxial deformation. The detwinning state was almost completely retained during unloading but was mainly reversed by heating above the phase transition temperature. These direct observations of the detwinning process of variants allow us to understand better the deformation mechanisms in SMAs used as sensors or actuators.

ACKNOWLEDGMENTS

This work is supported by the National Natural Science Foundation of China (Contract Nos. 50725102 and 50531020), the 111 Project (Contract No. B07015), the Cultivation Fund of the Key Scientific and Technical Innovation Project (Ministry of Education of China) (Contract No. 707017), and the Swedish Research Council in the frame of the SIDA project (Contract No. 348-2004-3475). The authors are also grateful for the support provided by the European Commission under the 6th Framework Programme through the Key Action: Strengthening the European Research Area, Research Infrastructures (Contract No. HII3-CT-2003-505). The use of the Advanced Photon Source was supported by the U.S. Department of Energy, Office of Science, Office of

Basic Energy Science under Contract No. DE-AC02-06CH11357.

- ¹K. Ullakko, J. K. Huang, C. Kantner, R. C. O'Handley, and V. V. Kokorin, *Appl. Phys. Lett.* **69**, 1966 (1996).
- ²V. A. Chernenko, V. L'vov, J. Pons, and E. Cesari, *J. Appl. Phys.* **93**, 2394 (2003).
- ³A. Sozinov, A. A. Likhachev, N. Lanska, and K. Ullakko, *Appl. Phys. Lett.* **80**, 1746 (2002).
- ⁴S. Sun, C. B. Murray, D. Weller, L. Folks, and A. Moser, *Science* **287**, 1989 (2000).
- ⁵K. Oikawa, W. Ito, Y. Imano, Y. Sutou, R. Kainuma, K. Ishida, S. Okamoto, O. Kitakami, and T. Kanomata, *Appl. Phys. Lett.* **88**, 122507 (2006).
- ⁶R. Kainuma, Y. Imano, W. Ito, Y. Sutou, H. Morito, S. Okamoto, O. Kitakami, K. Oikawa, A. Fujita, T. Kanomata, and K. Ishida, *Nature (London)* **439**, 957 (2006).
- ⁷R. C. O'Handley and S. M. Allen, in *Encyclopedia of Smart Materials*, edited by M. Schwartz (Wiley, New York, 2001).
- ⁸Y. Liu, Z. Xie, J. V. Humbeeck, and L. Delaey, *Scr. Mater.* **41**, 1273 (1999).
- ⁹A. A. Likhachev and K. Ullakko, *Phys. Lett. A* **275**, 142 (2000).
- ¹⁰P. Šittner, P. Lukáš, V. Novák, M. R. Daymond, and G. M. Swallowe, *Mater. Sci. Eng., A* **378**, 97 (2004).
- ¹¹C. R. Rathod, B. Clausen, M. A. M. Bourke, and R. Vaidyanathan, *Appl. Phys. Lett.* **88**, 201919 (2006).
- ¹²E. C. Oliver, T. Mori, M. R. Daymond, and P. J. Withers, *Acta Mater.* **51**, 6453 (2003).
- ¹³E. C. Oliver, T. Mori, M. R. Daymond, and P. J. Withers, *Scr. Mater.* **53**, 609 (2005).
- ¹⁴Y. D. Wang, D. W. Brown, H. Choo, P. K. Liaw, D. Y. Cong, M. L. Benson, and L. Zuo, *Phys. Rev. B* **75**, 174404 (2007).
- ¹⁵Y. D. Wang, Y. Ren, H. Li, H. Choo, M. L. Benson, D. W. Brown, P. K. Liaw, L. Zuo, G. Wang, D. E. Brown, and E. E. Alp, *Adv. Mater. Weinheim, Ger.* **18**, 2392 (2006).
- ¹⁶Y. D. Wang, Y. Ren, E. W. Huang, Z. H. Nie, G. Wang, Y. D. Liu, J. N. Deng, L. Zuo, H. Choo, P. K. Liaw, and D. E. Brown, *Appl. Phys. Lett.* **90**, 101917 (2007).
- ¹⁷I. Glavatsky, N. Glavatska, I. Urubkov, J.-U. Hoffman, and F. Bourdarot, *Mater. Sci. Eng., A* **481**, 298 (2008).
- ¹⁸D. Y. Cong, P. Zetterström, Y. D. Wang, R. Delaplane, R. L. Peng, X. Zhao, and L. Zuo, *Appl. Phys. Lett.* **87**, 111906 (2005).
- ¹⁹M. R. Daymond and H. G. Priesmeyer, *Acta Mater.* **50**, 1613 (2002).
- ²⁰A. C. Larson and R. B. Von Dreele, "General structure analysis system (GSAS)," Los Alamos National Laboratory Report No. LAUR 86-748, 2004.
- ²¹Y. D. Wang, Y. D. Liu, J. Z. Xu, and Z. D. Liang, *J. Appl. Phys.* **79**, 7376 (1996).
- ²²D. Y. Cong, Y. D. Zhang, Y. D. Wang, M. Humbert, X. Zhao, L. Zuo, and C. Esling, *Acta Mater.* **55**, 4731 (2007).
- ²³Y. Liu, *Proc. SPIE* **4234**, 82 (2001).